AUTOMATED REDUCTION OF FALSE POSITIVES AND FEATURE EXTRACTION OF COVID-19 IN 3D USING CHEST CT IMAGES

Aravind Jadhav[1]*, Dr. Sanjay Pujari[2]

Abstract

Many therapeutic and diagnostic procedures typically involve the use of CT imaging. When direct measurements of quality are required to analyze various patients kinds' signs and symptoms, location of the person's residence, and travel history, including close contact with any Covid-19 patient, it is the most effective and efficient tool for covid-19 diagnostic and therapeutic techniques. The segmentation procedure is crucial to CT diagnostic imaging. However, it can be difficult to tell the difference between symptoms and chest-related problems in pulmonary diagnostic CT imaging. The approach to decrease false positives for covid-19 recognition and to obtain useful structural data for lung diagnosis was proposed in this paper and experimentally tested. The first step is to segment the lungs of the interesting item using the morphological operation and thresholding approach of Otsu. Second, the 3D morphological feature-based parameters for covid-19 detection are measured. False positive reduction uses innovative SAV ratio-based thresholding as well as volume-based thresholding to remove undesired disturbances. The output identified significant structural data for the diagnosis of the lungs, (surface-area-to-volume ratio, volume, location, and density of covid-19 effect). Ten patients with covid-19 instances have their digitized transverse abdominal CT scans statistically examined and validated. To obtain validated data for the analysis, the expert radiologists separately estimated the coordinate points in the covid-19 region. With 95% overall accuracy, the suggested method greatly decreased false positives. Additionally, it can convey important details about the lung region affected by COVID-19.

Keywords: Covid-19, SAV ratio-based thresholding, volume-based thresholding, and feature extraction.

[1]*Departmentof E&CE, Angadi Institute of Technology and Management, Belagavi, Karnataka, India,
Email: jadhav.aravind@gmail.com
[2]Department of E&CE, KLE College of Engineering & Technology, Chikodi, Belagavi, Karnataka, India.
Email: pujarisap@gmail.com

*Correspondence Author: Aravind Jadhav
*Departmentof E&CE, Angadi Institute of Technology and Management, Belagavi, Karnataka, India.
Email: jadhav.aravind@gmail.com

I. Introduction

The recently identified coronavirus is the cause of the deadly COVID-19 illness. The coronavirus (SARS-COV-2) first infected a human in December 2019. It spreads mostly among people by droplets released during speaking, coughing, or sneezing by an infected individual [1-6]. The droplets are too heavy to go very far, so they cannot transmit from one person to another without making intimate contact [7]. According to a recent study, COVID-19 can survive for up to 3 hours in the air, 4 hours on copper, and 5 hours on plastic and stainless steel for up to 72 hours, however, the actual time is still unknown.However, the broader health research community is still at odds with the precise

solutions to these questions, which are currently being looked into. The technician's competence has a significant role in the accuracy of ultrasound imaging. However, a CT scan provides a greater contrast image that can show the interior shape from different planes and angles, as well as their size, density, and texture. Internal body structures can be seen on a CT scan without any overlapping structures [1]. The shape of the stone is visible in each slice of a 2D CT scan, as shown in Fig. 1(a), which is now being investigated by the medical community. The technician's competence has a significant role in the accuracy of ultrasound imaging.However, a CT scan provides a greater contrast image that can show interior shape,

Eur. Chem. Bull. **2023**, *12(Regular Issue 5), 5806 –5817*

5806

dimension, solidity, and appearance as well as their structure from various planes as well as angles. Internal body structures can be seen on a CT scan without any overlapping structures [1]. The stone's form is depicted in each 2D CT scan slice as seen in Fig. 1. (a). CT imaging computer-assisted detection can handle many situations with the same level of accuracy. The initial step in managing Covid-19 disease is to make a diagnosis using information from a CT scan [2]. Since diagnosing on 2D slices by scrolling upwardas well as downward takes time, 3D diagnostic imaging technology on CT data is now advancing to disclose customers' true anatomy more unambiguousand exactly. Both human and automated segmentation strategies have been employed in pre-processing using the very popular algorithm for a 3D display of CT data. Both segmentation methods have benefits and drawbacks. On the other side, manual and semi-automatic procedures take a lot of attention to detail, are time-consuming, need some training, and are not sensitive to noise.Fully automatic approaches operate with great repeatability and without the need for training, but they are prone to errors due to their sensitivity to noise and unforeseen circumstances [3]. Although there has been some study on segmenting abdominal organs from CT scan images, such as the liver, Covid-19, and spleen, the value of thresholding is restricted because different organs and tissues have relatively similar grey levels [4]. Given that the stone, stent, calcification, and bone have comparable grey levels [5], as seen in Fig. 1, it is challenging to tell them apart. Covid-19 segmentation on CT imaging has also proven to challenge (b). To extract features for automated Covid-19 detection, it is essential to use the feature parameter without grey-level values.

2. Literature Review

Deep learning algorithms have recently been used by researchers to study and evaluate chest X-ray pictures in order to identify COVID-19. The photos are initially pre-processed using the CNN technique to provide stronger features before being put into deep learning algorithms for image categorization.

Ahammed et.al [29] suggested a method based on deep neural networks that achieve great (94.03%) accuracy from CNN. The algorithm was trained by the authors using chest X-rays from COVID-19 patients with pneumonia and normal conditions. The work had a drawback in that it developed the system using a dataset of just 285 photos, which

was insufficient for preparing a deep learning-based COVID-19 forecastsystem.

Chowdhury et. al. [30] developed PD COVID Net, a unique framework based on parallel-dilated CNN, by making use of patients' chest X-ray images. The researchers employed a parallel stack with a dilated convolution that could capture and stretch data to reach a detection accuracy of 96.58% of the required information.

Abbas [31] proposed and validated identifying the decompose, transfer, and compose (DeTraC) deep convolution neural network that was utilized to extract the chest X-ray pictures of patients having COVID-19. To evaluate class boundaries and achieve excellent accuracy (93.1%) and sensitivity (100%) they proposed a decomposition approach while checking abnormalities from the dataset.

A deep learning method based on the CNN ResNet-101 model was used, according to Azemin [32]. Thousands of photographs were used in their suggested strategy to identify significant things during the pre-training phase and to spot abnormalities in chest filmsduring the re-training stage. The accuracy rate for this strategy was 71.9%.

El Rashidy [33] presented a three-tier framework with a cloud, hospital, and patient layer. A set of data was collected from the patient layer using a smartphone app and a few wearable sensors. A deep learning model based on neural networks was trained using the patient's X-ray scans to:recognize COVID-19. The proposed model had a 98.85% specificity rate and a 97.9% accuracy rate.

A databank of 307 pictures with four various classes—COVID-19, normal, pneumonia bacterial, and pneumonia virus—was utilized to train three deep transfer models, including AlexNet, GoogleNet, and ResNet18 in the proposed model by Loey et al. [35]. In order to save memory and speed up the execution of the study, it was divided into three scenarios. GoogleNet attained 99.9% validation accuracy and 100% testing accuracy in the prior deep transfer model.

Minaee [36] developed a deep learning-based system that uses ResNet18, ResNet50, SqueezeNet, and DensNet-121 are four tuning models used to identify COVID-19 in chest X-ray pictures. By applying data augmentation to create

Eur. Chem. Bull. **2023**, *12(Regular Issue 5), 5806 –5817*

5807

a modified version of the COVID-19 images, the suggested method climbssome numeral of samples and ultimately reached 98% sensitivity as well as 90% specificity.

Wang A [38] created a model that uses fusion effects between ResNet-101 and ResNet-151 to increase their load distribution effectively. Three kinds of chest X-ray images were created: normal, COVID-19, and viral infection. A qualitative part of 96.1% was achieved throughout testing.

Yoo et al. [39] applying a deeplearning-based decision-tree classifier to chest X-ray radiography (CXR) pictures allowed for the detection of COVID-19. Based on the PyTorch frame, three binary decision trees were compared by this classifier. The third decision tree has an average classification accuracy of 95% for CXR pictures.

3. Methodology

3.1 Theoretical mathematics

The volume of a sphere and the use of image processing techniques were used to construct the proposed algorithm. Thresholding and ratio were calculated for image pre-processing approaches based on geometrical concepts and the 3D selected Covid impacted region. The following section provides a summary of several works on 3D morphological measurement-based segmentation and feature extraction.

3.2 Image segmentation

Image segmentation, referred to as "pixel classification," splits a source image into several areas or parts (sets of pixels). A few features or computed attributes in each pixel in a region, such colour, intensity, or texture [17]. Four main categories of picture segmentation algorithms are listed below:
1. Segmentation based on edges.
2. Segmentation based on regions.
3. Segmentation based on graph cuts.
4. Segmentation based on thresholds.

My suggested approach uses thresholding-based segmentation among them because local pixel intensity levels are the foundation of the threshold technique. A single threshold value can be used to divide both regions because the intensity distribution between the affected area and the background (other organs) is seen. A threshold value selection for segmentation is simple when the background and foreground pixels of an image

differs sufficiently from one another. Of all the segmentation techniques now in use, it is the simplest, fastest, and easiest. Finding a suitable threshold, however, that can instantly divide the images into two groups is challenging [18 &19]. The main issue with thresholding is that we only take into account pixel relationships in terms of intensity. Due to an insufficient threshold value, it might occasionally happen because too many areas are lost and too many background pixels are obtained that are not necessary [20].

a) Morphological process: Morphology is a large category of techniques for manipulating shapes in images. The purpose of utilizing morphological operations is to improve the image's structural integrity. Morphological erosion and dilatation are two fundamental morphological processes: erosion normally destroys small things, while the succeeding dilation usually restores the shape of the objects that are still present. Most of the surgeries progress by a mix of erosion and dilation. For visual segmentation, morphological opening and filling are widely used in binary images and intensity-based images [22].

b) Morphological opening: The relationship between open pictures is determined by a combination of the operations of erosion and dilation. It can remove any tiny extensions that are there, clear any little bridges, and smooth the object's shape. One of the simplest ways to close gaps in a closed boundary is through morphological filling is by morphological filling (ROI). A collection of background pixels that cannot be filled in by starting from the image's edge are referred to as holes in this syntax. Utilizing the optional argument "holes," the Matlab toolbox function "imfill" automatically completes this calculation. A smoothing of the segmented object's surface can be a morphological filling.

3.3 Feature extraction for D shapes

The technique of feature extraction is used to necessary data from an image to complete computational tasks. Following are some of the features computed from the segmented Covid affected region using 3D voxel-based morphology:

a) Area

A fundamental variable in the extraction of 3D form characteristics is object area. The size of an area that is affected by Covid is determined by counting the number of voxels there [23]. Number of voxels in the object times area.

Eur. Chem. Bull. **2023**, *12(Regular Issue 5), 5806 –5817*

5808

b) The size of the affected area by COVID-19

Volume estimation is more precise and informative for the 3D shape of Covid-19 than stone diameter measurement [24]. By multiplying the 3D impacted area's area by the voxel resolution, the affected area's volume is calculated (voxel spacing).

Volume (V) = Resolution Area -------------- (1)

c) Surface Area of affected by COVID-19

$$SA = \sqrt{(x - res_x)2 + (y - res_y)2 + (z - res_z)2} .... (2)$$

Where, SA: surface area of stone res_x, , res_z: the resolution of the voxel in the X, Y, and Z direction.

d) Volume of a sphere

According to the following equation, the volume of a sphere can be estimated based on its radius.

$$Volume\ of\ sphere: V = \frac{4}{3}\pi r^3$$ ---------------------
(3)

Where V is the sphere's volume and r is its radius

Since the majority of Covid has asymmetrical shapes, volume estimation using the stone's surface area makes more sense than calculation using radius. The link between a sphere's radius and surface area:

$$Surface\ Area\ (SA) = 4\pi r^2$$ --------------------- (4)

As a result, the formula for a sphere's volume is as follows:

$$Volume\ of\ sphere: V = \sqrt{\frac{(SA)^3}{36\pi}}$$ ---------------------
(5)

Where V: is the volume of a sphere, and SA: is the surface area of a sphere

e) Surface-area-to-volume ratio, or SAV

According to [26], the effect of isoperimetric inequality in 3D objects is connected to an object's SAV ratio or surface area to volume ratio. The SAV ratio makes it possible to determine a 3D object's form. More differences in shape exist between items whose SAV are farther apart. The SAV of a spherical shape is the smallest, while the

One of the key elements in gaining access to the Covid component is the surface area of the impacted Covid area. Image resolution, which is a 1-by-3 row vector with resolution in the X, Y, and Z directions, is used to determine the surface area of the 3D binary structure (in that order). By comparing the calculated surface area to the theoretical value of the sphere's surface area, this calculation's accuracy is demonstrated.($4\pi r2$) in [25].

SAV of a triangular (tetrahedron) shape is the largest. A spherical-shaped object's SAV ratio is typically determined as follows.

$$SAV = \frac{3}{r}$$ --------------------- (6)

Where r is the sphere's radius

But the volume of the object is also taken into account when calculating SAV, not just its radius. Thus, the following formula for the SAV ratio can be used:

$$SAV_{sphere} = \frac{4.836}{\sqrt[3]{V}}$$ --------------------- (7)

where SAV is the stone's surface area and V is the Covid area's volume. Additionally, the segmented surface area and volume of the affected area can be used to estimate the SAV ratio.

$$SAV_{stone} = \frac{Surface\ area\ of\ stone}{Volume\ of\ stone}$$ --------------------- (8)

f) Ratio Volume Sphere (RVS)

By comparing 3D-reconstructed Covid volumes with the volume of a spheroid utilizing the diameter of the Covid region, the average Covid region area was predicted [27]. For branching analysis, the 3D ROI manager generated a relative volume ellipsoid in [28]. (RVE). RVS is the volume of the test object divided by the volume of a sphere having a surface area equal to that of the test item. Because the volume of the segmented Covid impacted area is larger than the volume of a sphere with a similar surface area, the stone has an irregular form structure and some of it has branches. RVS of no branches as a result.
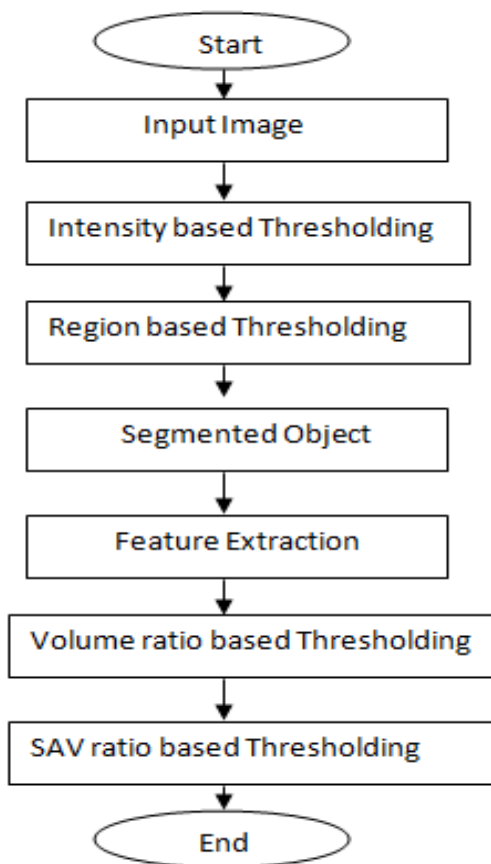
Eur. Chem. Bull. **2023**, *12(Regular Issue 5), 5806 –5817*

5809

Figure 1: The proposed 3D Covid area segmentation and false positive reduction stone range between 0 and 1, while the RVS of branches stone exceeds 1.

$$RVS = \frac{V_{obj}}{V_{sph}}$$

---------------------- (9)

Where: Test object's volume (the selected covid region)

Vsph denotes the volume of a sphere with the same surface area as the test object.

3.4 Datasets Preparations

A 14-slice CT scanner was used to capture the digitized transverse abdomen CT scan pictures from 15 patients with Covid cases at K L E Medical College in Belagavi. Each patient receives between 25 and 30 slices during their CT scan, depending on the conditions and varying Covid instances. Various Covid severe cases with calcification, stents, and without restrictions in the affected area make up the dataset used in this experimental study. The assessment of coordinate points in the lung place by skilled radiologists demonstrated the proposed algorithm's accuracy and efficacy. Furthermore, the proposed method output clarity has been compared to the results of recent research and software available for purchase (RadiAnt DICOM Viewer).
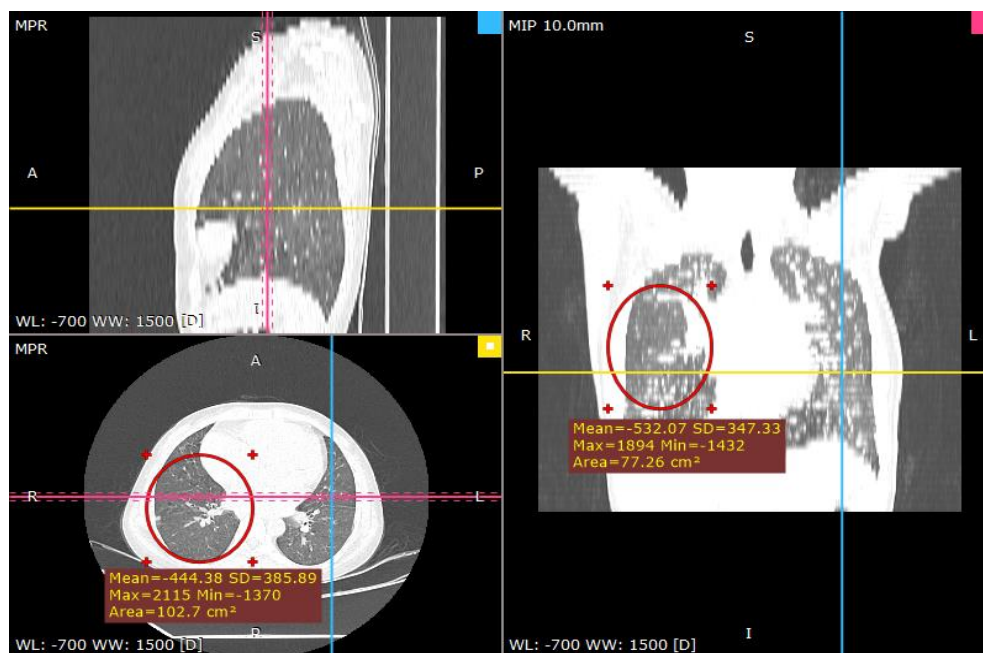
Eur. Chem. Bull. 2023, 12(Regular Issue 5), 5806 –5817

5810

Figure 2: The experimental results for Covid segmentation and false positive reduction (using the suggested algorithm) are shown in the (a) segmented result after low-intensity region removal, (b) segmented result after big region removal, and (c) segmented outcome following false positive elimination.

3.5 Proposed Method

The segmented 3D object shown in Fig. 2 is used to demonstrate automated noise removal and feature extraction approaches. These techniques use the thresholding methodology. These were used in the suggested approach to producing three different kinds of levels of image analysis (segmentation, false positive lowering, stentand big noise eliminating, and segmentation enhancement of the Covid region). The Covid affected area was segmented without losing the necessary information by first entering all the patient's slices into the computer and then removing the undesired regions from the CT scan image. The remaining noise from segmented output was then similarly eliminated towards lower false positives.

To remove most of the noise, the proposed technique was used to assess every object that was still present, regardless of whether it was in a Covid-affected area or not. The program will remove items from the image if there is a tube or significant noise.

4. Results and discussion

4.1 Implementation specifics
The following software implementation is suggested in this research for picture Otsu's thresholding, morphological operation, and 3D morphological feature extraction were used for segmentation and false positive reduction. To determine the necessary threshold values for each

step, Table 2's feature extraction from 3D segmented objects and prior knowledge of CT scan images were used. Segmenting Covid areas at 4.2 (pre-processing) The noise removal strategy uses Otsu's thresholding and morphological operation at the pre-processing stage. The segmentation process is begun by loading the input DICOM file. Thresholding based on intensity: Otsu's thresholding is the best technique for Covid-19 segmentation since the lungs and other low-intensity organs have unique intensity ranges. to small ones with low-intensity values, large objects with high-intensity value areas were simpler to identify and segment.Therefore, utilizing Otsu's thresholding and morphological operation, the lung can be extracted among other soft tissue and organs, enhancing the output image [29]. As demonstrated in Fig. 2, this segmentation can only contain high-intensity regions and cannot eliminate low-intensity regions (a). Localized thresholding Affected Covid regions come in sizes ranging from small (the size of a sand grain) to huge (the size of golf balls). In comparison to other objects, the skeletal bones (including the ribs, spinal column, and pelvic bone) have a high voxel density. Therefore, area-based thresholding is used to remove the bone skeleton from the image. Each object's area can be determined using Eq (2). The position of Covid-19 in the lungs is also confined in the inner of the bony skeleton, and a bed mat is present behind the bony skeleton and stone due to the nature of CT scanning in the Covid-19 case. For the location-based thresholding approach, the estimation of two

coordinate thresholding values has been used [30]. Bony skeleton and certain bone fragments are eliminated from the image as a result of the pre-processing. However, as demonstrated in Fig. 2, some portion of the noise from segmentation error, calcification, and stent are still present alongside the afflicted area (b). To separate the region from other undesired noise, a false positive reduction is therefore carried out.

4.3 Reduced false positives

Feature extraction: From the segmentation output image, the fundamental 3D morphological features (area, volume, and surface area of the stone object) are first computed. The volume of the sphere is also determined in order to calculate the volume ratio. The ratio Volume Sphere (RVS) and SAV ratio are designed as effective and efficient noise abatement features. Small noise reduction: A 3D item's shape can be predicted by comparing the volume of the object to the volume of a sphere, or RVS. Typically, noise forms (non-effected areas) have a fiber-like appearance with RVS values between 1 and 2. Consequently, adopting RVS-based thresholding can eliminate the fiber-shaped non-affected areas (with two threshold values, 1 and 2). There are several different types of Covid affected areas, including those with rounded, spherical, oval, and stag horn shapes. In some areas, especially those with a wide affected area, the surface is frequently uneven and has branches. The small, affected area is rounded, without any branches, and has a smooth surface. As a result, the branching, the small, segmented area can be low-level noise (fiber-shaped noise). As seen in Fig. 2, RVS can lessen fiber-shaped noise from the segmented output (c). Stents and loud noise abatement Sometimes, after removing the fiber-shaped non-affected area, the stent is left as noise. Using intensity and size features to remove the stent from the lungs is challenging.Due to the disparities in their shapes, the suggested study used SAV-based thresholding. There is a distinct gap when SAV of a more affected region is compared to SAV of a sphere, despite there being a modest difference in SAV value between big noise, stent, and affected area (standard SAV).

5. Experimental results

Abdominal CT images based on the incidence of Covid affected areas were used as the basis for the data analysis for this investigation. The tests were performed on a computer with an Intel® Core (TM).
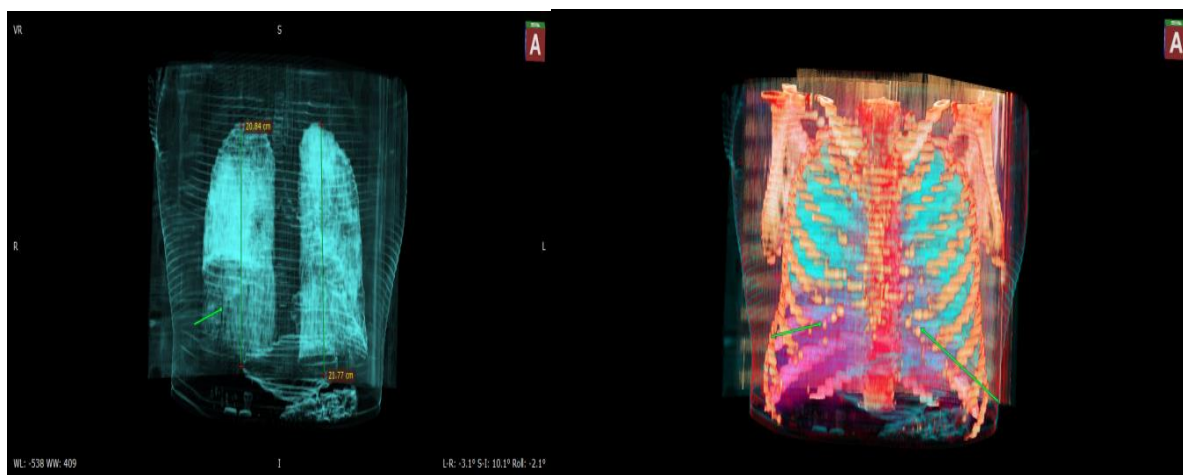

Fig3: a) 3D visualization from the segmented output using the suggested algorithm, b) Application RadiAnt DICOM Viewer (64-bit).

5.1 D Visualization

A crucial component of Covid-19 diagnosis is the visualization of CT data. In this study, surface data from a 3D volume array is extracted using a Matlab program for its surfaces. In Fig. 3, segmented output was viewed in three dimensions using the proposed algorithm in (a) and the RadiAnt DICOM Viewer (64-bit) application in (b). proposed algorithm through a comparison of RadiAnt DICOM Viewer's (64-bit) object. The object can be resolved by delaying the mouse on the plane to see all sides of the Covid affected area. When compared to RadiAnt DICOM Viewer's output, the proposed technique can clearly and noise-free display the more affected area, as shown in Fig. 3. This experiment demonstrates how the suggested technique can produce a 3D output image with the maximum clarity and the least amount of noise.

Eur. Chem. Bull. **2023**, *12(Regular Issue 5), 5806 –5817*
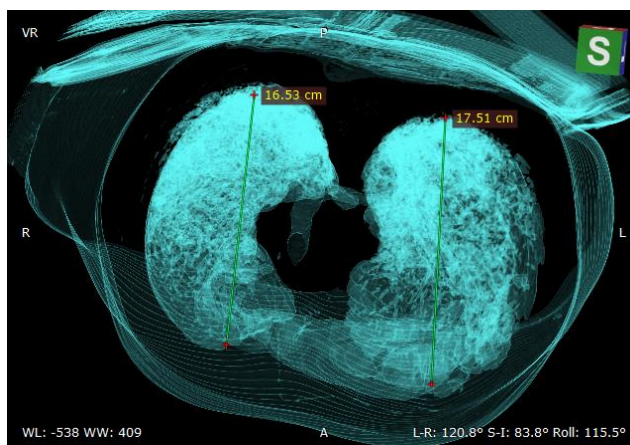
5812

5.2 Segmentation result

Figure. 4: 3D visualization of segmented output more affected area clearly without any disturbances.

To segment the Covid afflicted area on CTcovid images, we created a fully automatic computer-aided diagnosis method. The suggested technique can identify various lung abnormalities in 15 individuals, and RadiAnt DICOM Viewer can show various sections of the same database. As seen in Fig. 4, the suggested approach can remove numerous undesirable items that RadiAnt DICOM Viewer is unable to remove. In addition, compared to RadiAnt DICOM Viewer, more affected regions are segregated using the suggested approach, going from 53 to 69. Consequently, 69 true positives and 78 false positives were found in the segmentation results using the suggested algorithm, which is a 20% difference from RadiAnt DICOM Viewer.
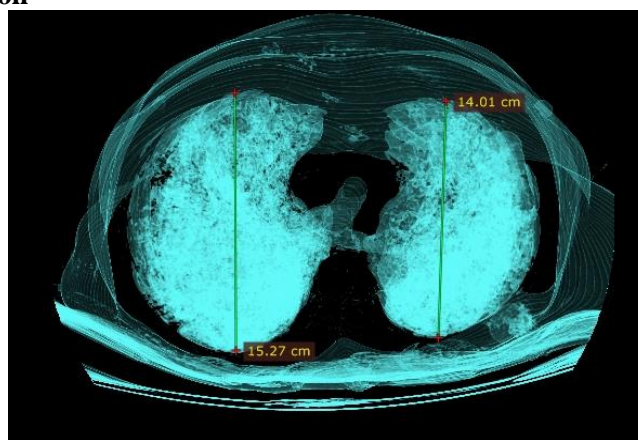
5.3 Performance evaluation

Figure. 5: 3D visualization of Performance Evaluation

Figure 5 displays a 3D visualization of performance evaluation; in this study, sensitivity was utilized to compare various algorithms. It is calculated in [31] using the TP and FN rate as displayed below:

$$\text{Sensitivity} = \frac{TP}{TP+FN} \quad \text{----------------------} \ (10)$$

Covid-affected areas, which are appropriately identified as having severe Covid, are treated with TP. For non-affected Covid areas that are discovered from the lung area, FN is applied. The manual record and program outputareorganized to validate the achievementof the suggested algorithm. Table 1 presents the experimental results for attainment appraisal, with sensitivity determined using Eq (12). The sensitivity of the three processes in the suggested algorithm was 45%, 68%, and 79%, respectively. These techniques are reported to extract Covid with a sizable true positive detection rate. Covid diagnosis is provided with a fair output image, even though, still there are some false negatives. RVS and SAV ratio were two effective techniques offered by the suggested algorithm to lower the incidence of false positives. In comparison to the segmentation results, RVS reduces most false positives (particularly small fiber-shape non-stone items) by roughly 70%. SAV ratio can identify big

Eur. Chem. Bull. **2023**, *12(Regular Issue 5), 5806 –5817*

5813

false positives among the stones, increasing system accuracy by up to 70%.

5.4 Output information

The proposed algorithm produced a text file as an additional output for 3D visualization. The meaningful structural data of the text file includes the stone's location (left, right, or chest), the size of the lung (area and volume), and the typical density of the affected Covid area (Hounsfield unit). Three CT images of the chest are displayed in the output information in Figure 6. Using Eqs. (2) and (3), the volume and area were measured (3). Next, using the formulas below, the average density of the area affected by COVID was determined.

$$Average\ HU = \frac{Total\ value\ HU\ of\ the\ object}{Number\ of\ pixels\ of\ an\ objects} \quad (11)$$
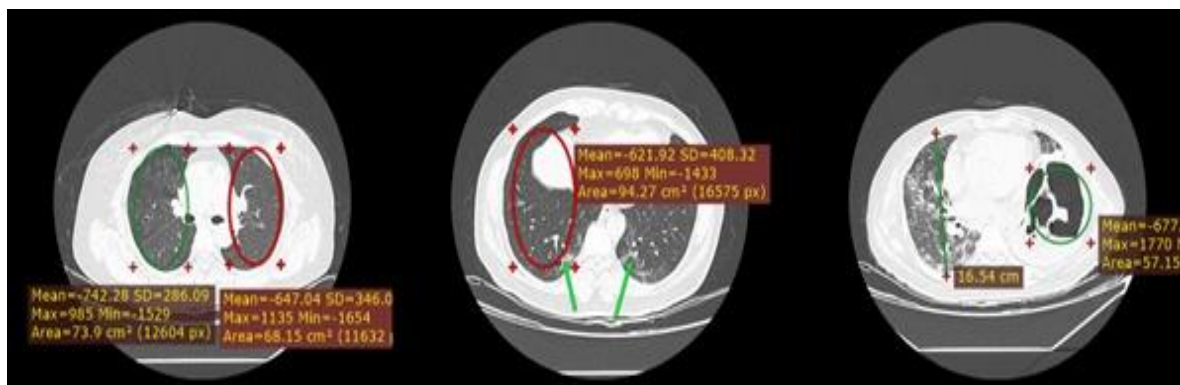

Figure.6: Output information of three Chest CT images

Table: 1: Performance evaluation

S.no	Chest CTImage-1	Chest CTImage-2	Chest CTImage-3
1	Mean=742.28.54	Mean=621.92	Mean=677.4
2	Max=985	Max =698	Max =1770
3	Area=73.9cm	Area=94.27cm	Area=57.15cm
4	SD=286.09	SD=408.32	SD=181.87

6. Conclusion and future work

On CT images, we created a segmentation tool for the Covid-19 affected area that is entirely automatic computer-aided diagnosis. The uniqueness of my proposed study is the use of segmenting every slice of the object and extracting features from the 3D matrix (3D morphological feature). Considering the visualization results, the suggested segmentation algorithm produced output images that were more clear than those produced by earlier studies using RadiAnt DICOM Viewer. Additionally, it can segment the afflicted area, whereas RadiAnt DICOM Viewer only segments 53 stones. The similarity in Covid's affected area's size, shape, and level of noise was the primary factor in the reduction of false positives. To overcome the issue of image noise in this situation, we additionally produced the following two effective features (RSV and SAV ratio features). By lowering image noise in the segmented output, these RVS and SAV ratios, two proposed features, improve anenticingquality of a computer-aided diagnosis system. According to manual examination, there are two types of noise in the segmented output: small, fiber-shaped noise and huge noise are tough to differentiatebetween partial and more affected areas. Among the true positive stones, the fiber-shaped noise can be effectively extracted utilizing the ideal threshold range generated using the RVS feature. Because of a gap in SAV between the affected and unaffected area, SAV is especially useful for large noise and stent removal. As a result, as illustrated in Table 3, the suggested or projected false reduction technique based on RVS and SAV characteristics can reduce the number of false negatives from 70 to 25. Although the proposed segmentation algorithm can segment some minor affected Covid areas that the RadiAnt DICOM Viewer cannot display, its accuracy was only moderately high. As a result, we implemented and validated acorrect operation based on the appraisal of coordinate points in the affected area determined separately by qualified radiologists. Table 3 shows that the sensitivities of each method are 45%, 60%, and 79%, respectively, at 10 patients on the test dataset. The technique also can autonomously split the affected COVID area, enabling false reduction based on 3D morphological features. The technique can offer useful information for CT scan

Eur. Chem. Bull. **2023**, *12(Regular Issue 5), 5806 –5817*

5814

interpretation, such as covid position, affected region, and affected density. This work only demonstrated the clean extraction of a 3D coherent object; its resilience is still lacking. To create the most accurate approach for diagnosing COVID-19, we, therefore, intend to investigate more durable segmentation and feature extraction algorithms.

References

1. A. K. Mishra, S. K. Das, P. Roy, and S. Bandyopadhyay, "Identifying COVID-19 from chest CT images: A deep convolutional neural networks-based approach," Journal of Healthcare Engineering, vol. 2020, p. 8843664, Aug 2020.

2. Stones Analyses in Computed Tomography Images". 'IEEE International Conference on Innovations in Engineering, Technology and Sciences (ICIETS), NIE Institute of Technology Mysore,20th, and 21st September 2018.

3. S. Heidarian, P. Afshar, N. Enshaei, F. Naderkhani, A. Oikonomou, S. F. Atashzar, F. B. Fard, K. Samimi, K. N. Plataniotis, A. Mohammadi, and M. J. Rafiee, "COVID-FACT: A fully-automated capsule network based framework for identification of COVID-19 casesfrom chest CT scans," pp. 1–16, Sep 2020.

4. P. Afshar, S. Heidarian, N. Enshaei, F. Naderkhani, M. J. Rafiee, A. Oikonomou, F. B. Fard, K. Samimi, K. N. Plataniotis, and A. Mohammadi, "COVID-CT-MD: COVID-19 computed tomography (CT) scan dataset applicable in machine learning and deep learning," pp. 1–9, Sep 2020.

5. S. P. Singh, L. Wang, S. Gupta, H. Goli, P. Padmanabhan, and B. Guly´as, "3D deep learning on medical images:A review," Oct 2020.

6. M. Fang, B. He, L. Li, D. Dong, X. Yang, C. Li, L. Meng, L. Zhong, H. Li, H. Li, et al., "Ct radiomics can help screen the coronavirus disease 2019 (covid-19): a preliminary study," Science ChinaInformation Sciences, vol. 63, no. 7, 2020.

7. H. J. Chen, Y. Chen, L. Yuan, F. Wang, L. Mao, X. Li, Q. Cai, J. Qiu, J. Tian, and F. Chen, "Machine learning-based ct radiomics model distinguishescovid-19 from other viral pneumonia," 2020.

8. Q. Wu, S. Wang, L. Li, Q. Wu, W. Qian, Y. Hu, L. Li, X. Zhou, H. Ma, H. Li, et al., "Radiomics analysis of computed tomography helps predict poor prognostic outcome in

9. covid-19," Theranostics, vol. 10, no. 16,p. 7231, 2020.

10. Yang R, Li X, Liu H. et al. Chest CT Severity Score: An Imaging Tool for Assessing Severe COVID-19. RadiolCardiothorac Imaging.2020 ;2:e200047

11. Gong J, Ou J, Qiu X. et al. A Tool to Early Predict Severe 2019-Novel Coronavirus Pneumonia (COVID-19) : A Multicenter Study using the Risk Nomogram in Wuhan and Guangdong, China. medRxiv. 2020. 2020 03.17.20037515. doi: https://doi.org/10.1101/2020.03.17.20037515

12. Wynants L, Van Calster B, Bonten MMJ. et al. Prediction models for diagnosis and prognosis of covid-19 infection: Systematic review and critical appraisal. BMJ. 2020;369:m1328

13. Arentz M, Yim E, Klaff L. et al. Characteristics and Outcomes of 21 Critically Ill Patients With COVID-19 in Washington State. JAMA. 2020;323:1612-1614

14. Shi H, Han X, Jiang N. et al. Radiological findings from 81 patients with COVID-19 pneumonia in Wuhan, China: a descriptive study. Lancet Infect Dis. 2020;20:425-434

15. Li K, Wu J, Wu F. et al. The Clinical and Chest CT Features Associated with Severe and Critical COVID-19 Pneumonia. Invest Radiol. 2020;55:327-331

16. Li Q, Guan X, Wu P. et al. Early Transmission Dynamics in Wuhan, China, of Novel Coronavirus-Infected Pneumonia. N Engl J Med. 2020;382:1199-1207

17. Zhou F, Yu T, Du R. et al. Clinical course and risk factors for mortality of adult inpatients with COVID-19 in Wuhan, China: a retrospective cohort study. Lancet. 2020;395:1054-1062

18. Wang D, Hu B, Hu C. et al. Clinical Characteristics of 138 Hospitalized Patients with 2019 Novel Coronavirus-Infected Pneumonia in Wuhan, China. JAMA. 2020;323:1061-1069

19. Yang X, Yu Y, Xu J. et al. Clinical course and outcomes of critically ill patients with SARS-CoV-2 pneumonia in Wuhan, China: a single-centered, retrospective, observational study. Lancet Respir Med. 2020;8:475-481

20. Yang R, Li X, Liu H. et al. Chest CT Severity Score: An Imaging Tool for Assessing Severe COVID-19. RadiolCardiothorac Imaging. 2020;2:e200047

21. Qi X, Jiang Z, YU Q. et al. Machine learning-based CT radiomics model for predicting

Eur. Chem. Bull. **2023**, *12(Regular Issue 5), 5806 –5817*

5815

hospital stay in patients with pneumonia associated with SARS-CoV-2 infection: A multicenter study. medRxiv. 2020. 2020 02.29.20029603. doi: https://doi.org/10.1101/2020.02.29.20029603

21. Yan L, Zhang H-T, Goncalves J. et al. A machine learning-based model for survival prediction in patients with severe COVID-19 infection. medRxiv. 2020. 2020 02.27.20028027. doi: https://doi.org/10.1101/2020.02.27.20028027

22. Wynants L, Van Calster B, Bonten MMJ. et al. Prediction models for diagnosis and prognosis of covid-19 infection: Systematic review and critical appraisal. BMJ. 2020;369:m1328

23. World Health Organization. Coronavirus disease 2019(COVID-19): Weekly Epidemiological and Operationalupdates October 2020. Geneva: WHO, 2020.

24. Zhou F, Yu T, Du R, et al. Clinical course and riskfactors for mortality of adult inpatients with COVID-19in Wuhan, China: a retrospective cohort study. Lancet2020;395:1054–1062.

25. Shi H, Han X, Jiang N, et al. Radiological findings from81 patients with COVID-19 pneumonia in Wuhan,China: a descriptive study. Lancet Infect Dis2020;20:425–434.

26. Yu Q, Wang Y, Huang S, et al. Multicenter cohort studydemonstrates more consolidation in upper lungs on ini-tial CT increases the risk of adverse clinical outcome inCOVID-19 patients. Theranostics 2020;10:5641–5648

27. Larue R, van Timmeren JE, de Jong EEC, et al. Influenceofgray level discretization on radiomic feature stabilityfor different CT scanners, tube currents and slice thick-nesses: a comprehensive phantom study. Acta Oncol2017;56:1544–1553

28. Song L, Zhu Z, Mao L, et al. Clinical, conventional CTand radiomic feature-based machine learning models forpredicting ALK rearrangement status in lung adenocar-cinoma patients. Front Oncol 2020;10:369

29. uo D, Gu D, Wang H, et al. Radiomics analysis enablesrecurrence prediction for hepatocellular carcinoma afterliver transplantation. Eur J Radiol 2019;2117:33–40

30. Duan YN, Qin J. Pre- and Posttreatment Chest CTFindings: 2019 Novel Coronavirus (2019-nCoV)Pneumonia. Radiology 2020;295:21.

31. Zhang R, Ouyang H, Fu L, et al. CT features of SARS-CoV-2 pneumonia according to

clinical presentation: aretrospective analysis of 120 consecutive patients fromWuhan city. EurRadiol 2020;30:4417–4426

32. Chen T, Wu D, Chen H, et al. Clinical characteristics of113 deceased patients with coronavirus disease 2019: ret-rospective study. BMJ 2020;368:m1091

33. Wu C, Chen X, Cai Y, et al. Risk factors associated withacute respiratory distress syndrome and death in patientswith coronavirus disease 2019 pneumonia in Wuhan,China. JAMA Intern Med 2020;180:934–943.

34. Guo D, Gu D, Wang H, et al. Radiomics analysis enablesrecurrence prediction for hepatocellular carcinoma afterliver transplantation. Eur J Radiol 2019;2117:33–40.

35. Zhang, J.-J.; Dong, X.; Cao, Y.-Y.; Yuan, Y.-D.; Yang, Y.-B.; Yan, Y.-Q.; Akdis, C.A.; Gao, Y.-D. Clinical Characteristics of 140 Patients Infected with SARS-CoV-2 in Wuhan, China. Allergy 2020, 75, 1730–1741

36. Huang, C.; Huang, L.; Wang, Y.; Li, X.; Ren, L.; Gu, X.; Kang, L.; Guo, L.; Liu, M.; Zhou, X.; et al. 6-Month Consequences of COVID-19 in Patients Discharged from Hospital: A Cohort Study. Lancet 2021, 397, 220–232.

37. Wang, Y.; Dong, C.; Hu, Y.; Li, C.; Ren, Q.; Zhang, X.; Shi, H.; Zhou, M. Temporal Changes of CT Findings in 90 Patients with COVID-19 Pneumonia: A Longitudinal Study. Radiology 2020, 296, E55–E64

38. The National Health Commision of the People's Republic of China. Diagnosis and Treatment Protocol for COVID-19 in China (Trial Fifth Edition). 8 February 2020.

39. Lambin, P.; Leijenaar, R.T.H.; Deist, T.M.; Peerlings, J.; de Jong, E.E.C.; van Timmeren, J.; Sanduleanu, S.; Larue, R.T.H.M.; Even, A.J.G.; Jochems, A.; et al. Radiomics: The Bridge between Medical Imaging and Personalized Medicine. Nat. Rev. Clin. Oncol. 2017, 14, 749–762.

40. Han, X.; Fan, Y.; Alwalid, O.; Li, N.; Jia, X.; Yuan, M.; Li, Y.; Cao, Y.; Gu, J.; Wu, H.; et al. Six-Month Follow-up Chest CT Findings after Severe COVID-19 Pneumonia. Radiology 2021, 299, E177–E186

41. Caruso, D.; Zerunian, M.; Polici, M.; Pucciarelli, F.; Polidori, T.; Rucci, C.; Guido, G.; Bracci, B.; De Dominicis, C.; Laghi, A. Chest CT Features of COVID-19 in Rome, Italy. Radiology 2020, 296, E79–E85

42. Ai, T.; Yang, Z.; Hou, H.; Zhan, C.; Chen, C.; Lv, W.; Tao, Q.; Sun, Z.; Xia, L. Correlation

Eur. Chem. Bull. **2023**, *12(Regular Issue 5), 5806 –5817*

5816

of Chest CT and RT-PCR Testing for Coronavirus Disease 2019 (COVID-19) in China: A Report of 1014 Cases. Radiology 2020, 296, E32–E40

43. Han, X.; Fan, Y.; Alwalid, O.; Zhang, X.; Jia, X.; Zheng, Y.; Shi, H. Fibrotic Interstitial Lung Abnormalities at 1-Year Follow-up CT after Severe COVID-19. Radiology 2021, 210972.

44. Li, L.; Wang, L.; Zeng, F.; Peng, G.; Ke, Z.; Liu, H.; Zha, Y. Development and Multicenter Validation of a CT-Based Radiomics Signature for Predicting Severe COVID-19 Pneumonia. Eur. Radiol. 2021, 31, 7901–7912

45. Kumar, V.; Gu, Y.; Basu, S.; Berglund, A.; Eschrich, S.A.; Schabath, M.B.; Forster, K.; Aerts, H.J.W.L.; Dekker, A.; Fenstermacher, D.; et al. Radiomics: The Process and the Challenges. Magn. Reson. Imaging 2012, 30, 1234–1248

46. Fang, X.; Li, X.; Bian, Y.; Ji, X.; Lu, J. Radiomics Nomogram for the Prediction of 2019 Novel Coronavirus Pneumonia Caused by SARS-CoV-2. Eur. Radiol. 2020, 30,

47. Wu, Q.; Wang, S.; Li, L.; Wu, Q.; Qian, W.; Hu, Y.; Li, L.; Zhou, X.; Ma, H.; Li, H.; et al. Radiomics Analysis of Computed Tomography Helps Predict Poor Prognostic Outcome in COVID-19. Theranostics 2020, 10, 7231–7244

48. Guan W-J, Ni Z-Y, Hu Y et al (2020) Clinical characteristics of coronavirus disease 2019 in China. N Engl J Med 382:1708– 1720. https://doi.org/10.1056/NEJMoa2002032

49. Santos MK, Ferreira Júnior JR, Wada DT, et al (2019) Artificial intelligence, machine learning, computer-aided diagnosis, and radiomics: advances in imaging towards precision medicine. Radiol Bras 52:387–396. https://doi.org/10.1590/0100-3984. 2019.0049

50. Meiler S, Schaible J, Poschenrieder F et al (2020) Can CT performed in the early disease phase predict the outcome of patients with COVID-19 pneumonia? Analysis of a cohort of 64 patients from Germany. Eur J Radiol 131:109256. https://doi.org/10. 1016/j.ejrad.2020.109256

Eur. Chem. Bull. **2023**, *12(Regular Issue 5), 5806 –5817*

5817